Signal Processing 165 (2019) 197–208

Contents lists available at ScienceDirect

Signal Processing

journal homepage: www.elsevier.com/locate/sigpro

Shadow removal based on separated illumination correction for urban aerial remote sensing images

Shuang Luo[a], Huanfeng Shen[a,b,c], Huifang Li[a,*], Yumin Chen[a]

[a] School of Resource and Environmental Sciences, Wuhan University, Wuhan, PR China
[b] Collaborative Innovation Center of Geospatial Technology, Wuhan, PR China
[c] Key Laboratory of Geographic Information System, Ministry of Education, Wuhan University, Wuhan, PR China

ARTICLE INFO

Article history:
Received 30 January 2019
Revised 10 June 2019
Accepted 30 June 2019
Available online 1 July 2019

Keywords:
Shadow removal
Spatially adaptive
Illumination correction
Aerial images

ABSTRACT

The presence of shadows in urban aerial images degrades the image quality and reduces the application accuracy. Removing shadows and recovering the ground information is therefore a crucial issue. The existing shadow removal methods can correct the shadow information, but the inconsistency between the corrected shadow and non-shadow areas is still obvious. A novel shadow removal method based on separated illumination correction is proposed in this paper, in which the shadow removal is only performed on the shadow-related illumination. A spatially adaptive weighted total variation model is constructed to obtain the shadow-related illumination and the shadow-free reflectance. The objects in the shadows are detected based on the reflectance, and object-oriented illumination correction is then implemented to compensate the shadow regions. The shadow removal results can be obtained by combining the corrected illumination and the reflectance. Three aerial remote sensing images were selected for the experiments, and two quantitative evaluation methods are introduced: the shadow standard deviation index and classification analysis. The results are shown and compared with four existing methods by visual and quantitative assessments, which indicate that the proposed method can yield more visually natural shadow-free images and show a better performance in the quantitative indices.

1. Introduction

Shadows are a natural phenomenon, occurring when direct light is totally or partially occluded by objects, and they exist in most aerial remote sensing images. According to the shadow location, shadows can be divided into cast shadow (the part that is cast on the ground by high objects) and self-shadow (the part of the object that is not illuminated). Cast shadow is the concern of this paper. With the improvement of the spatial resolution of remote sensing images, the shadow effect in remote sensing images is becoming more and more obvious [1–4]. Shadows can be used to reconstruct three-dimensional information, but shadows also cause radiometric information reduction, which makes the image interpretation more difficult [5–10]. In high spatial resolution imagery of urban environments, the shadow effect is more serious because the surface features are quite complex, with a great variety of objects such as high buildings, trees, and so on [11–14]. It is therefore essential to remove the shadow effect to improve the amount and the quality of the image radiometric information.

A variety of shadow removal methods have been proposed in the past decades, especially for close-shot images. These methods can be divided into two main categories: local color transfer methods and global optimization methods. The local color transfer methods take advantage of the spatial similarity to construct a relationship between the intensity of the paired shadows and non-shadows by a color transfer technique, to restore the shadow regions, where the existing relationship is mainly composed of linear correlation, statistical correlation, gamma function, and machine learning. Considering the linear relationship between shadows and non-shadows, the linear-correlation correction method has been proposed and widely used in recent years [2,13,15–21]. As a common image enhancement method, the histogram matching method has been adopted to remove shadows, where shadow pixels are recovered by matching the histogram of the shadow regions to that of the non-shadow areas [11,15,22,23]. The gamma correction method has also been used to correct shadow regions by using a power function to construct the relationship between shadow and non-shadow pixels [15,24–26]. In recent years, machine learning has been introduced to build the relationship between shadow and non-shadow pixels by the use of a Markov random field (MRF) model [27]. Above all, the local color transfer methods can correct the shadow information, to some extent, but the corrected

* Corresponding author.
E-mail address: huifangli@whu.edu.cn (H. Li).

https://doi.org/10.1016/j.sigpro.2019.06.039
0165-1684/

results are usually inconsistent with the non-shadow areas and show serious shadow boundary effects, because mismatching often occurs between the shadow and non-shadow regions due to the low brightness of shadows. On the other hand, as the land-cover types are more complex in remote sensing images than close-shot images, the paired samples are usually selected by visual judgment, in order to ensure the matching accuracy.

The global optimization methods take the whole image into consideration directly, and compensate the information of shadow regions through global optimization. These methods include the Poisson correction method, variational models, and deep learning based methods. The Poisson correction method reconstructs a shadow-free image based on the corrected gradient information by nullifying the gradients on shadow boundaries through the Poisson equation [28,29], but the textural information in the boundaries is lost due to the totally zero gradients. Owing to the extensibility and precision, a number of variational models have been proposed to remove shadows by eliminating the shadow intensity component in the observed images [30–33]. However, the results are highly dependent on the estimation of the shadow intensity, and eliminating the shadow intensity totally always results in the loss of color information. As deep learning has shown obvious advantages in image processing in recent years, it has also been introduced to learn the relationship between the shadow image and shadow-free image by constructing an end-to-end deep convolutional neural network [34–36]. However, the deep learning based methods need a large number of shadow and real corresponding shadow-free image pairs for training, which is difficult to realize for remote sensing images due to the limitation of the data acquisition approaches. In conclusion, the global optimization methods can remove the shadows in whole directly, but they are not good at restoring the details of the image. For high-resolution remote sensing images, different land surfaces are covered by shadow, the spatial details are more complex than for close-shot images, and the penumbras can be significant, which are issues that are often ignored by the global optimization methods.

From the above analysis, the main problems encountered when removing shadows from aerial remote sensing images can be summarized as follows: (1) the accurate matching between shadow and non-shadow pairs is difficult, due to information attenuation in the shadow regions; (2) the complex spatial details in the shadow areas of high-resolution remote sensing images make shadow removal difficult; and (3) serious boundary effects usually exist in the shadow removal results, owing to the improper handling of the penumbra regions.

In order to solve the existing problems, we propose a novel shadow removal algorithm based on separated illumination correction, which combines the advantages of local color transfer and global optimization. Global optimization is utilized to separate the structured illumination, and local color transfer is only performed on the shadow-related illumination, to avoid the problems caused by the complexity of the reflectance. On the other hand, in consideration of the global smoothness of the illumination, local Gaussian smoothing is performed on the illumination to eliminate the shadow boundary effects in the shadow removal results effectively. The shadow mask is detected in advance by the shadow matting method [33,37]. It should be stressed that we focus on the shadows cast on the ground, while self-shadows located on buildings are not considered. Moreover, few of the existing shadow removal methods have evaluated their results quantitatively, as no shadow-free ground truth is available. Two different quantitative analysis methods are introduced in this paper to further evaluate the proposed shadow removal method: the shadow standard deviation index (SSDI) and classification analysis.

The main contributions and advantages of our work can be summarized as follows:

(1) A novel separated illumination correction algorithm is proposed to remove shadows for urban aerial remote sensing images, which can yield visually natural shadow-free images without obvious shadow boundaries.
(2) A spatially adaptive weighted total variation model is constructed to separate the structured illumination and shadow-free reflectance, and the object-oriented local color transfer is used to correct the shadow information in the illumination.
(3) SSDI and classification analysis are introduced to evaluate the shadow removal results quantitatively.

The rest of this paper is organized as follows. Section 2 explains in detail the innovative method developed for shadow removal. Section 3 presents the experimental analysis, including the results obtained by the proposed method and four existing methods on three urban remote sensing images. Finally, we conclude the paper in Section 4.

2. Methods

According to retinex theory [38], an observed image S can be represented as the product of two different components, i.e., the reflectance R and the illumination L, which can be expressed as:

$$S(x, y) = R(x, y) \cdot L(x, y) \tag{1}$$

where (x, y) denotes the pixel position, $R(x, y) \in [0, 1]$, and $L(x, y) \in (0, \infty)$. The reflectance R is a shadow-free variable, describing the objective properties of the observed ground. The illumination L contributes to the global brightness variation, which is related to the light illuminating the objects with smooth spatial variation.

For shadow images, the shadow spatial and spectral information are both included in the illumination which is shadow-related, and the texture and edge details of the ground are included in the reflectance which is shadow-free. Shadow removal aims to compensate the illuminating light and enhance the information in shadow regions. The separation of the shadow-related illumination and the shadow-free reflectance provides us a good opportunity to remove the shadow influence independently while maintaining the ground information. Therefore, a separated illumination correction based shadow removal method is proposed in this paper. Since the illumination is shadow-related, it is piecewise smooth, with obvious shadow structure, called structured illumination. The variational model is constructed to estimate the structured illumination, and land cover adaptive local color transfer is used to compensate the illumination in the shadows by an object-oriented strategy. The specific process flow of the proposed method is shown in Fig. 1.

2.1. Structured illumination estimation

Based on the above retinex theory, estimating the illumination or reflectance from the degraded image is a crucial task, but it is an ill-posed inverse problem. It is standard to use a regularization technique to make an inverse problem well posed, which can be formulated as a variational problem, and a globally optimized solution can be obtained by minimizing the energy function [39–41]. On the other hand, the flexibility and expandability of the variational model provide convenience for the structured variables [42–46]. Therefore, in consideration to the illumination spatial feature, we propose the spatially adaptive weighted total variation (SAWTV) model to estimate the structured illumination.

Based on the above analysis, a number of basic assumptions are put forward: (1) the illumination is close to the observed image from the global radiance view; (2) the reflectance is noise free; and (3) the illumination is structured and noise free. In order to simplify the computation, Eq. (1) is converted into the log domain

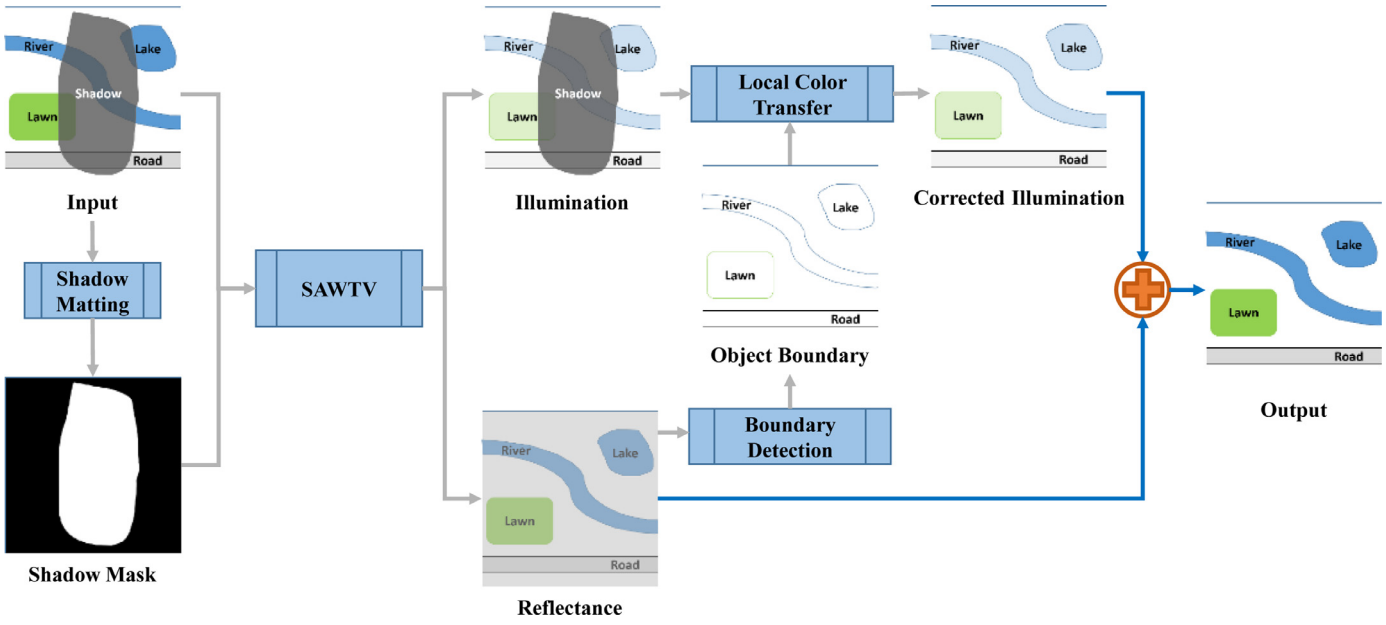

Fig. 1. Flowchart of shadow removal based on separated illumination correction for urban aerial remote sensing images.

as $s(x,y) = r(x,y) + l(x,y)$. Therefore, the SAWTV model is constructed as:

$$\hat{l} = \underset{l}{\operatorname{argmin}} \|l - s\|_2^2 + \alpha \|\nabla(l - s)\|_2^2 + \beta W \|\nabla l\|_{TV} \tag{2}$$

where the first fidelity term enforces the proximity between l and s; the second term enforces the spatial smoothness of the reflectance; and the third term is the weighted total variation (TV) regularization, which enforces the piecewise smoothness and the significant structure of the illumination. α and β are positive parameters, which control the contribution of each term in the model. The piecewise smoothness of the illumination is separated by the spatial distribution of the shadow, i.e., the shadow and non-shadow regions are both smooth, while the spatial structure of the shadow is preserved clearly. Therefore, we construct a weighted TV regularization term to constrain the illumination, which has a weak constraint on the shadow boundary, and otherwise has a strong constraint. The shadow boundary is decided by the gradient of the previous detected shadow mask, and thus the weight parameter W is defined as:

$$W(x,y) = \frac{1}{\delta(x,y) + \varepsilon} \tag{3}$$

where $\delta(x, y)$ is the gradient magnitude of shadow boundary pixel (x, y) in the shadow image, and ε is a small number, which is used to avoid the denominator being zero.

Split Bregman iteration [47] is employed to solve the optimization problem of Eq. (2), to ensure the calculation efficiency and stability. Hence, the structured illumination containing the shadow information and the shadow-free reflectance are both obtained.

2.2. Object-oriented illumination correction

Since the illumination contains the spatial and spectral information of the shadow, locally compensating the shadow regions in the illumination can effectively remove the shadows. As the illumination is piecewise smooth, the correction of the illumination can avoid the error caused by complex land cover, when compared to direct correction on the observed image. However, the illumination varies with different land-cover types, even under the same illumination conditions, which cannot be ignored. Therefore, we utilize an object-oriented strategy, i.e., the different objects in the shadow regions are corrected by taking the corresponding non-shadow objects as references, to obtain the land-cover related and shadow-free illumination.

How to identify the objects in shadow regions is the key. Radiation is usually weak in the shadow regions of an observed image, which makes Digital Number (DN)- or radiation-based classification difficult, but the land-cover boundaries in the shadow regions are usually obvious, and are well preserved in the reflectance. Therefore, we can effectively obtain the objects in the shadow regions and non-shadow regions through extracting the land-cover boundaries in the reflectance, and we construct the connected relationship between shadow objects and non-shadow objects to achieve the matching of shadow and non-shadow pairs.

In the same remote sensing image, if objects in a shadow region and a non-shadow region belong roughly to the same land-cover type, a linear relationship should exist between them [7,15,17,48]. As the shadow-related information is included in the illumination, the linear relationship between a shadow region and a non-shadow region is also suitable for the illumination. Based on the above assumption, we compensate the shadow information using the non-shadow information of the same land-cover type with the local color transfer method. Since the illumination is smooth, it has no strict requirement for the matching accuracy, and the object-oriented strategy proposed in this paper can satisfy the requirement of the illumination correction. The moment matching [49] is conducted in the illumination, which can be expressed as follows:

$$l_{corr} = \frac{\sigma_{ns}}{\sigma_s}(l - \mu_s) + \mu_{ns} \tag{4}$$

where l_{corr} is the gray value of the corrected result, and l is the gray value of the shadow objects. μ_s and μ_{ns} are the mean values of the shadow regions and non-shadow regions, respectively. σ_s and σ_{ns} are the standard deviation of the shadow regions and non-shadow regions, respectively. After the local color transfer process, the shadows in the illumination can be removed.

However, the corrected illumination will exhibit artifacts around the shadow boundaries because of the penumbra. In consideration of the smoothness of the illumination, local Gaussian smoothing is adopted, which can effectively eliminate the artifacts and does not lead to the loss of texture information for the final

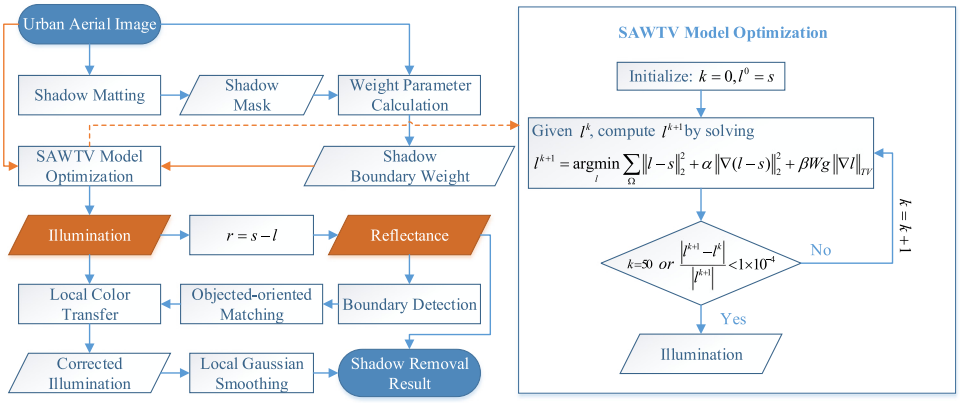

Fig. 2. Flowchart with computation details of the proposed method.

shadow-free image, because the texture and edge details of the ground are included in the reflectance. The final shadow removal result can be obtained by adding the corrected illumination to the reflectance, and then transforming to the spatial domain.

In order to make the proposed method more clearly, a flowchart with computational details is shown in Fig. 2.

2.3. Quantitative assessment methods

Although a few publicly available shadow removal datasets have been constructed for close-shot images [34,35,50,51], there are still no ground-truth shadow-free images available for remote sensing images, due to the limitation of the data acquisition approaches and the significant cost. Therefore, it is difficult to assess the shadow removal results of remote sensing images quantitatively. To solve this problem and make a quantitative analysis possible, we introduce the shadow standard deviation index (SSDI) and supervised classification.

In this paper, the SSDI σ_{s-ns} is based on the assumption that the same land-cover type in the same image should have similar gray values, which is defined as follows:

$$\sigma_{s-ns} = \frac{1}{B}\sum_{b=1}^{B}\sqrt{\frac{1}{N}\sum_{i=1}^{N}\left(F_{b,i}^{s} - \bar{F}_{b}^{ns}\right)^2} \tag{5}$$

where b is the current band of the image, and B is the total band number of the image. i is the current sample pixel in the shadow regions, and N is the total number of samples in the shadow regions. F^s is the corrected shadow sample set, and $\bar{F}^{ns}$ is the mean value of the corresponding non-shadow sample set of the same land-cover type.

The SSDI can reflect the variation of the corrected shadow regions with regard to homogeneous non-shadow regions. A low SSDI value indicates that the corrected shadow regions are consistent with the non-shadow regions, while a high SSDI value indicates that the corrected shadow regions show obvious differences with the non-shadow regions. For the SSDI, the shadow/non-shadow samples must satisfy the three following conditions: (1) the shadow/non-shadow samples should contain all the land-cover types in the shadow regions; (2) the non-shadow samples should be close to the corresponding shadow samples of the same land-cover type; and (3) the pixel numbers of the non-shadow samples should be approximately equal to the shadow samples.

To better analyze and compare the different shadow removal methods, the support vector machine (SVM) classification method [52] is also adopted as the other quantitative assessment method. The shadow removal results of the different methods are classified with the same non-shadow training samples, which are selected by visual interpretation. Four evaluation indices are used to evaluate the classification results: producer's accuracy (PA), user's accuracy (UA), overall accuracy (OA), and kappa coefficient (KC) [53,54]. PA is calculated through dividing the number of correctly classified samples of a certain category by the total number of ground truth samples of this category. UA is calculated through dividing the number of correctly classified samples of a certain category by the total number of samples classified in this category. OA is calculated through dividing the total number of correct classified samples of all categories by the total number of samples taken. KC is a robust measurement of how well the classification performs as compared to just randomly assigning values. For all these four indexes, a higher value indicates better performance.

3. Experiments

Three aerial remote sensing images with a ground resolution of around 0.20 m were selected to test the proposed shadow removal method. These images are all of urban residential areas, where the shadows are obvious. The dense high-rise buildings cast large shadows on the different land-cover types, such as roads, vegetation, lakes, and so on. The results of the proposed method are shown and compared with the results of four other shadow removal methods, which are linear-correlation correction (LCC) [15,48], histogram matching correction (HMC) [22], subregion matching illumination transfer (SMIT) [18], and spatially adaptive nonlocal regularization (SANL) [33]. LCC constructs a linear function to correct the shadow regions based on the non-shadow regions, while HMC employs the lookup table (LUT) technique in a two-step histogram matching approach to correct the shadow regions. These two methods do not consider different land-cover types in shadow regions and artifacts around the shadow boundaries in the shadow removal results. SMIT performs illumination transfer on the matched subregion pairs between the shadow regions and non-shadow regions, mainly focusing on the close-shot images which has smaller shadow regions and simpler land-cover types than remote sensing images. SANL removes shadows by regularizing the shadow scale and the updated shadow-free image, based on an initial shadow-free image estimated by the color transfer [49,55,56]. All these four comparison methods correct shadows directly, while the proposed method separates the illumination and reflectance from the original images, and makes the correction in the illumination.

To ensure that the comparison is reliable, we use the same shadow mask for all the shadow removal methods. In addition, two different quantitative measurements, i.e., the SSDI and supervised classification, are adopted to assess the results objectively.

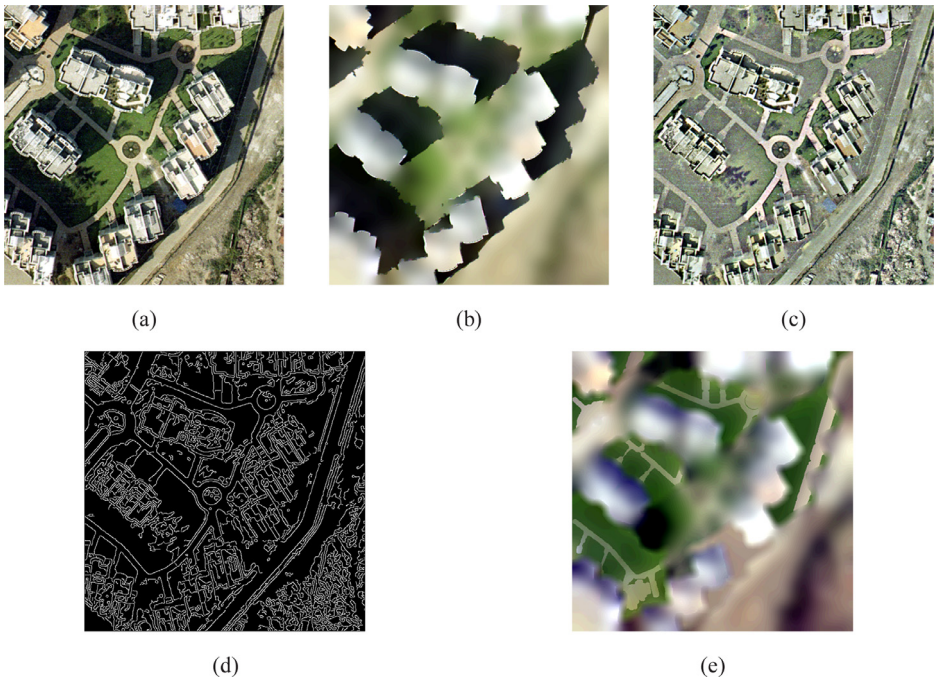

Fig. 3. Results of the proposed method for image #1. (a) Image #1. (b) The structure illumination. (c) The shadow-free reflectance. (d) The boundary detection result. (e) The illumination-corrected result.

Moreover, three parameters are involved in the proposed SAWTV model: α, β and ε. ε is empirically set to be 1×10^{-3} to avoid the denominator being zero. α and β are positive and balance the contributions of the three terms in the SAWTV model. α mainly controls the contributions of the first and second terms, i.e. approaching of the illumination to the original image and spatial smoothness of the reflectance, while β controls the contribution of the third term, i.e. piecewise smoothness of the illumination. Through a trial-and-error test, we set $\alpha = 10$, $\beta = 0.002$ to obtain structured illumination and shadow-free reflectance.

3.1. Visual comparison

Image #1 contains five main types of land cover, i.e., road, soil, building, vegetation, and shadow, as shown in Fig. 3(a). The illumination is piecewise smooth, with obvious shadow structure and spectral information, as shown in Fig. 3(b), while the reflectance is shadow-free, containing the texture and edge details of the ground, as shown in Fig. 3(c). We can see that the land-cover boundaries have been extracted accurately based on the reflectance, as shown in Fig. 3(d). The land-cover boundaries are then used to construct the connected relationship between shadow objects and non-shadow objects, to achieve the matching pairs. The shadow-related illumination is compensated well by the object-oriented local color transfer, as shown in Fig. 3(e). The final shadow removal result is shown in Fig. 4(e), where it can be seen that all the shadows have been removed. To make the result clearer, a detailed region is cropped from the shadow removal result in Fig. 5(e). It is clear that the spectral information and texture details in the corrected shadow regions are consistent with the non-shadow regions, while the shadow boundaries have been eliminated well, without obvious artifacts.

To compare the proposed method with the four other shadow removal methods, the shadow removal results and corresponding detailed regions are shown in Figs. 4 and 5, respectively. As shown in Figs. 4(a) and 5(a), the LCC method improves the brightness of the shadow regions, but the shadow boundaries are obvious and the noise is heavy. The road and vegetation in the recovered shadow regions are also inconsistent with the non-shadow regions. The results of the HMC method are shown in Figs. 4(b) and 5(b), where the shadow regions have been improved, but similar problems exist as with the LCC method. LCC and HMC methods both correct the shadow regions without consideration of the reflectivity difference between the different land-cover types, leading to the problem of the road being overcompensated and the vegetation undercompensated. Furthermore, the boundary artifacts are obvious because these two methods make no specific processing around the shadow boundaries. The results of the SMIT method are shown in Figs. 4(c) and 5(c), where the land-cover matching between the shadow region and non-shadow region is inaccurate, leading to a poor result because of the complexity of the remote sensing data and the distribution of the pixel values. However, the results could be improved in other ways, such as stretching the image before the matching operation. In this study, the shadow removal result of the SMIT method was directly generated on the original unstretched image to ensure that the comparison was reasonable. In the results of the SANL method shown in Figs. 4(d) and 5(d), the road and vegetation have been recovered well, but the boundaries of the shadow region are smoothed. The nonlocal regularization optimization is used to reduce the influence of noise and fake edges, but this also introduces texture detail blurring for the shadow-free result. Compared with the above methods, the proposed method can not only preserve the texture information well, such as road and vegetation, but it can also recover the illumination around the shadow boundaries.

The shadow removal results for the other two images are shown in Figs. 6 and 8, while Figs. 7 and 9 are detailed regions cropped from the two images. The shadow regions cast by the high-rise buildings are dense, containing complex land-cover types, i.e., road, soil, vegetation, and lake, as shown in Figs. 6(a) and 8(a). The LCC method corrects the shadow information, on the whole, in Figs. 6(b) and 8(b), but the shadow boundaries and brightness difference between shadow regions and non-shadow regions are obvious in Figs. 7(b) and 9(b). For the results of the HMC method, the brightness of the shadow regions is improved, but the roads in the

Fig. 4. Shadow removal results for image #1. (a) Result of the LCC method. (b) Result of the HMC method. (c) Result of the SMIT method. (d) Result of the SANL method. (e) Result of the proposed method.

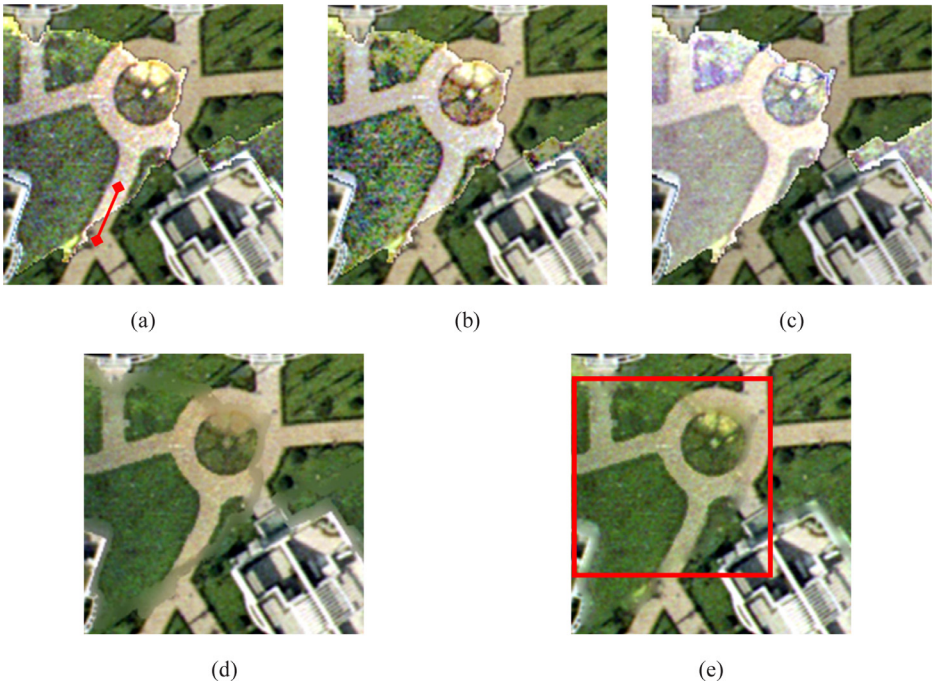

Fig. 5. Detailed regions cropped from Fig. 4. (a) Result of the LCC method. (b) Result of the HMC method. (c) Result of the SMIT method. (d) Result of the SANL method. (e) Result of the proposed method. (For interpretation of the references to color in this figure, the reader is referred to the web version of this article.)

shadow regions are undercompensated in Fig. 6(c) and overcompensated in Fig. 8(c). Moreover, the noise is enhanced, as shown in Figs. 7(c) and 9(c). The results of the SMIT method are overcompensated, and the color contrast between the different land-cover types in the shadow regions are not obvious in Figs. 6(d) and 8(d). For the results of the SANL method, the shadow regions are corrected well, with clear land-cover boundaries in Figs. 6(e) and 8(e); however, the texture detail is blurry and the shadow boundaries are smooth, as shown in Figs. 7(e) and 9(e). For the results of the proposed method, as shown in Figs. 6(f) and 8(f), the detailed information of the image is well recovered, without obvious shadow boundaries.

To investigate the shadow removal results in detail, we selected some typically homogeneous land-cover types around shadow boundaries to perform the profile analysis. The positions of the profile lines are labeled in red in Figs. 5(a), 7(a), and 9(a). Fig. 10(a)–(c) show the mean gray values of the three channels of the original image and the five shadow removal results.

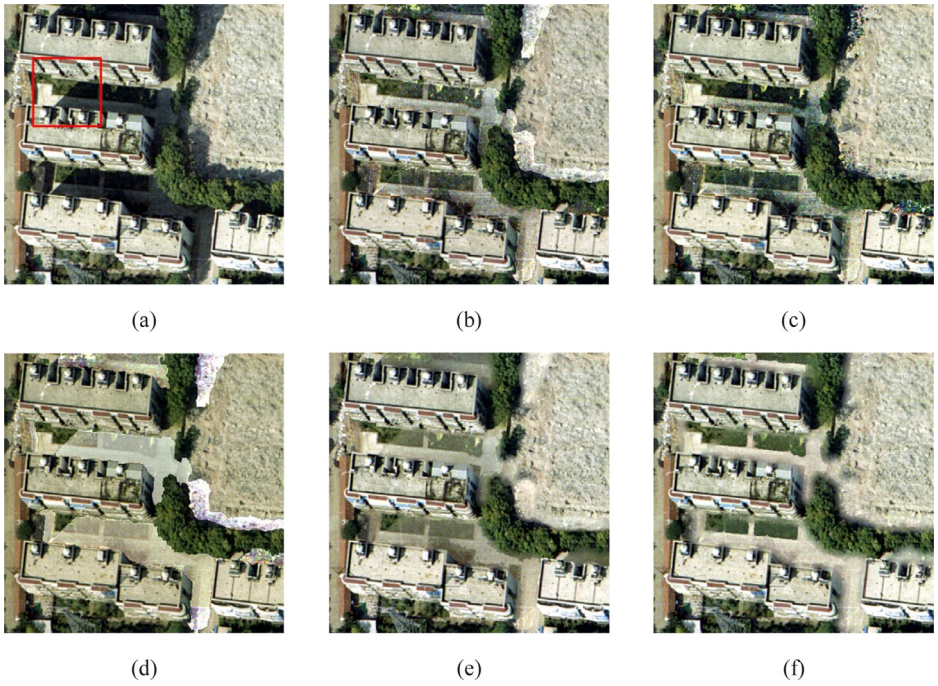

Fig. 6. Image #2 and its shadow removal results. (a) Original image with shadows. (b) Result of the LCC method. (c) Result of the HMC method. (d) Result of the SMIT method. (e) Result of the SANL method. (f) Result of the proposed method.

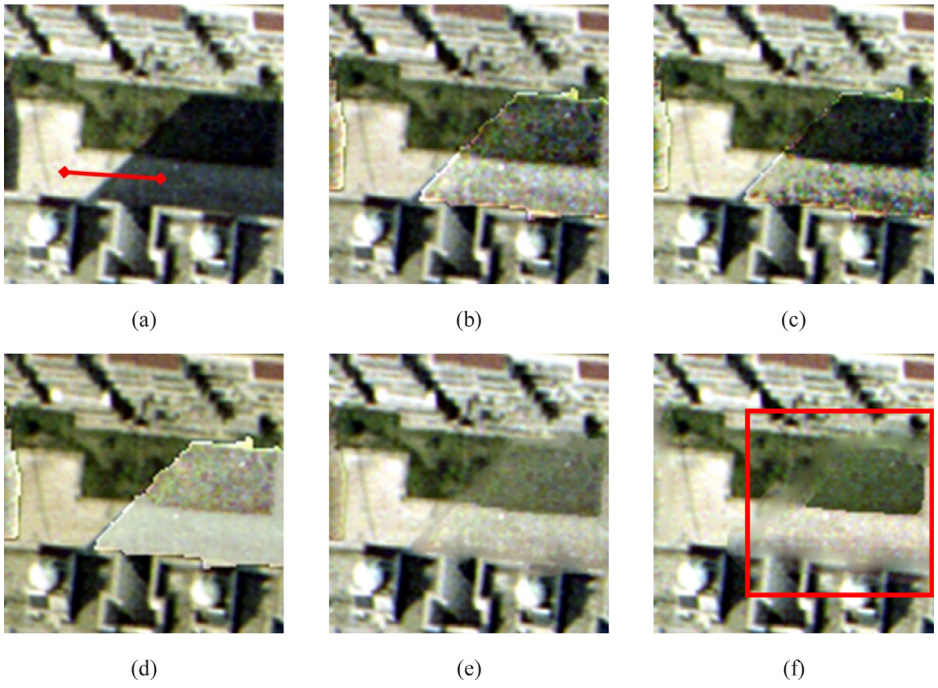

Fig. 7. Detailed regions cropped from Fig. 6. (a) Original image with shadows. (b) Result of the LCC method. (c) Result of the HMC method. (d) Result of the SMIT method. (e) Result of the SANL method. (f) Result of the proposed method. (For interpretation of the references to color in this figure, the reader is referred to the web version of this article.)

In the non-shadow parts of the profiles, the proposed method (red solid line) preserves the consistency with the original image (green solid line), without significant difference, while the SANL method (blue solid line) results in obvious fluctuations in Fig. 10(a), because of the nonlocal smoothing around the shadow boundaries. In the transitional parts of the profiles, the proposed method shows a smooth transition from non-shadow region to corrected shadow region, while the LCC method (magenta solid line), the HMC method (cyan solid line), and the SMIT method (black solid line) show drastic fluctuations in Fig. 10(a)–(c). In the shadow parts of the profiles, the proposed method shows a similar tendency to the non-shadow parts in Fig. 10(a)–(c), which means that the shadow removal results are more consistent with the surrounding non-shadow regions than those of the other methods. The proposed method also shows a good performance in the profile analysis of the corrected objects between the corrected shadow area and the non-shadow area.

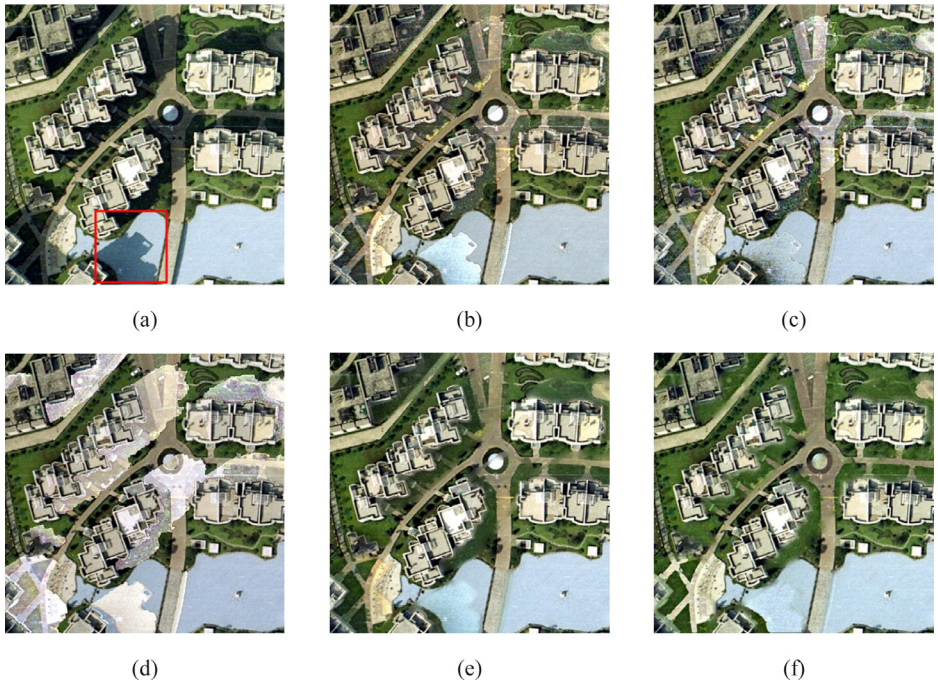

Fig. 8. Image #3 and its shadow removal results. (a) Original image with shadows. (b) Result of the LCC method. (c) Result of the HMC method. (d) Result of the SMIT method. (e) Result of the SANL method. (f) Result of the proposed method.

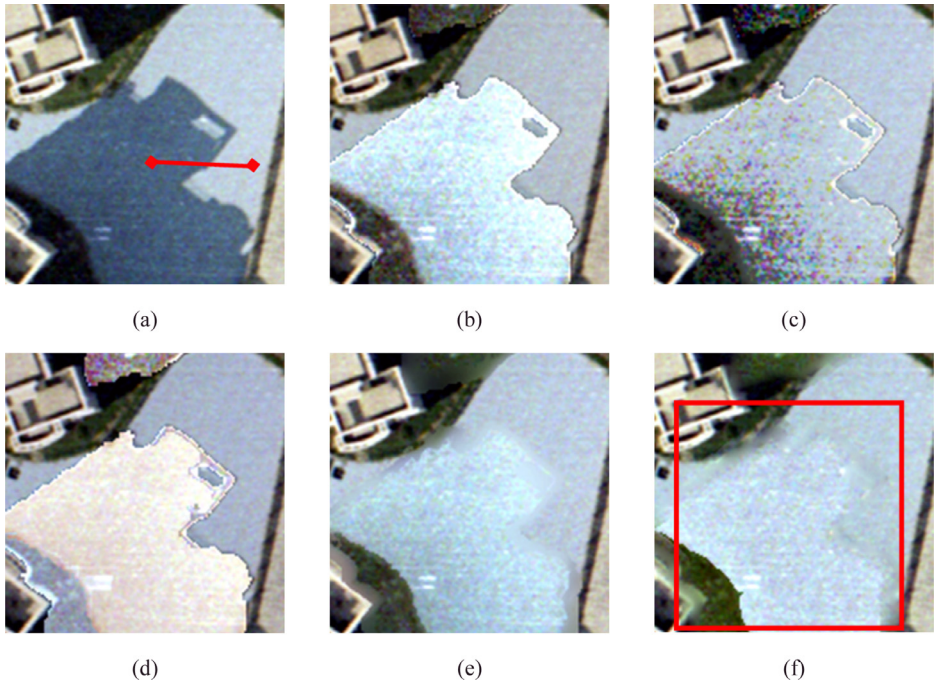

Fig. 9. Detailed regions cropped from Fig. 8. (a) Original image with shadows. (b) Result of the LCC method. (c) Result of the HMC method. (d) Result of the SMIT method. (e) Result of the SANL method. (f) Result of the proposed method. (For interpretation of the references to color in this figure, the reader is referred to the web version of this article.)

3.2. Quantitative assessment

In addition to the visual comparison of the shadow removal results, quantitative assessments were also carried out, including the SSDI and supervised classification. As the road and soil classes have similar spectral radiances for the three experimental images, these two land-cover types were classified as the same type. On the other hand, the assessments mainly focused on the land-cover types in the shadow regions, i.e., road, soil, vegetation, and lake.

According to the selection conditions for the shadow/non-shadow samples in Section 2.3, the SSDI values for the three reconstructed shadow images are calculated and listed in Table 1. It can be clearly seen that the SSDI of the proposed method is lower than those of the other methods for the different land-cover types, which means that the corrected shadow regions of the proposed method are more consistent with the non-shadow regions.

For the supervised classification of the shadow removal results, the first image is taken as an example to show the classification

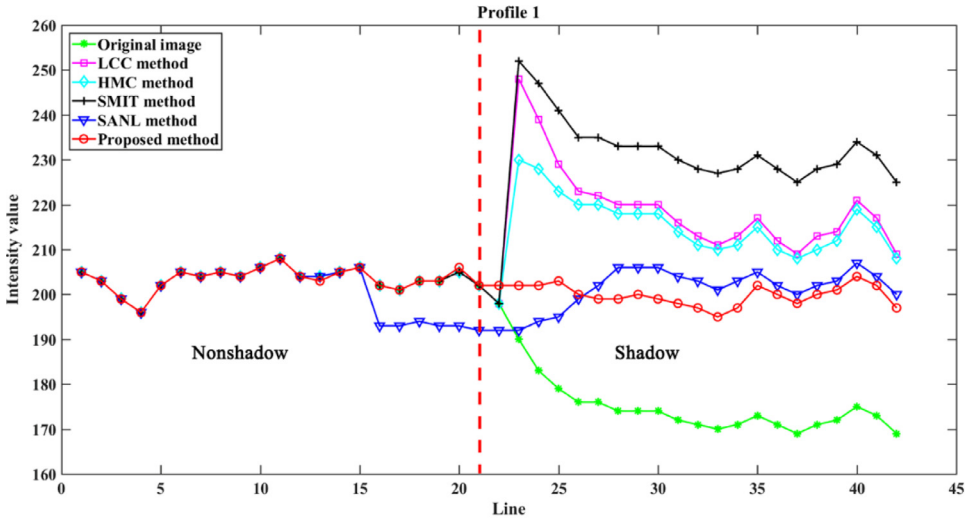

(a)

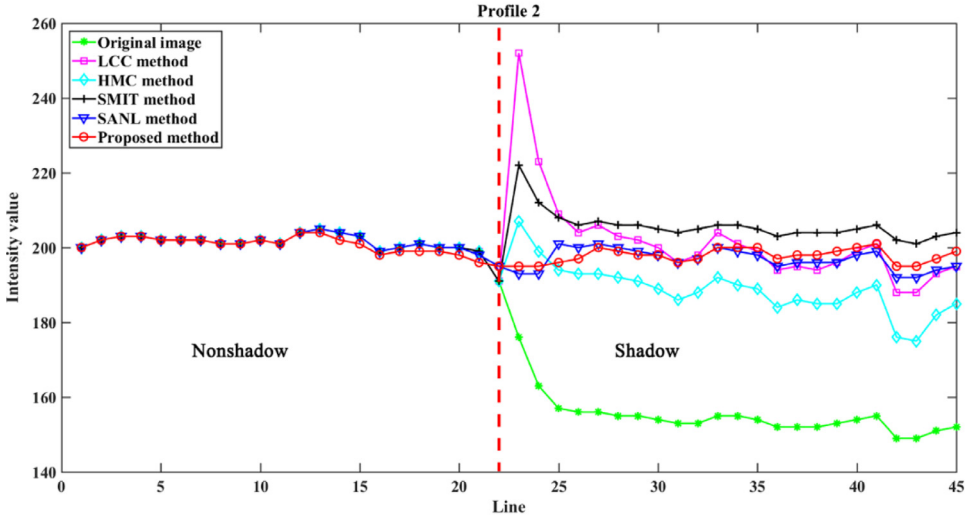

(b)

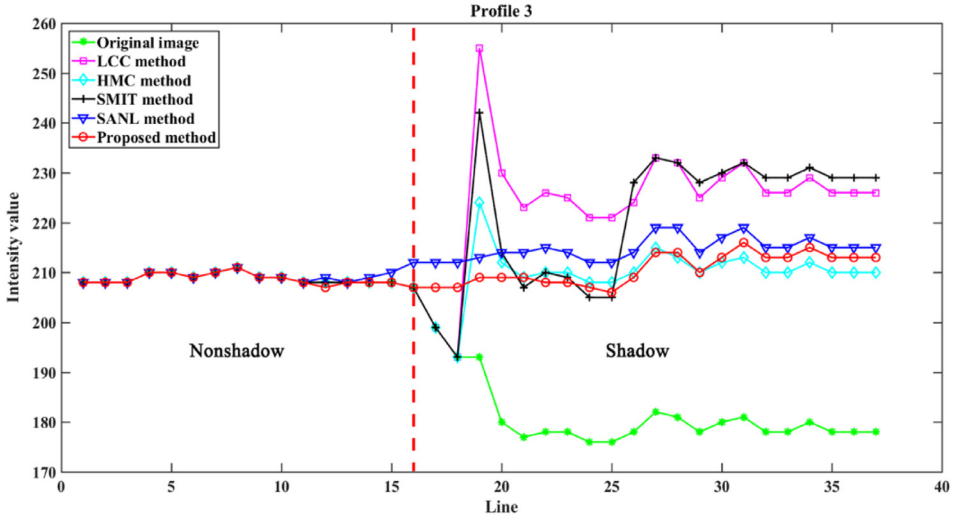

(c)

Fig. 10. Profile analysis of the three detailed regions in Figs. 5, 7 and 9. (a) Gray value profile of the corrected results for the detailed region in Fig. 5. (b) Gray value profile of the corrected results for the detailed region in Fig. 7. (c) Gray value profile of the corrected results for the detailed region in Fig. 9. (For interpretation of the references to color in this figure, the reader is referred to the web version of this article.)

Table 1
SSDI for selected samples from the three corrected shadow images.

Image	Class	Number of pixels		LCC	HMC	SMIT	SANL	Proposed
		Shadow	Non-shadow					
#1	Road and soil	2916	2910	11.3215	11.5619	25.7235	7.1971	**6.1307**
	Vegetation	4878	4882	7.4423	11.3972	28.5434	6.1534	**4.0823**
#2	Road and soil	4040	4049	12.7532	21.0429	13.7016	9.1964	**6.1452**
	Vegetation	2214	2128	7.0317	9.4139	31.7487	10.1001	**3.5922**
#3	Road and soil	2164	2148	9.7991	12.6977	26.2411	9.2691	**9.1817**
	Vegetation	3378	3395	7.4886	10.5659	33.4774	6.9627	**4.7923**
	Lake	1777	1765	11.4873	10.9168	14.1387	4.7043	**3.8091**

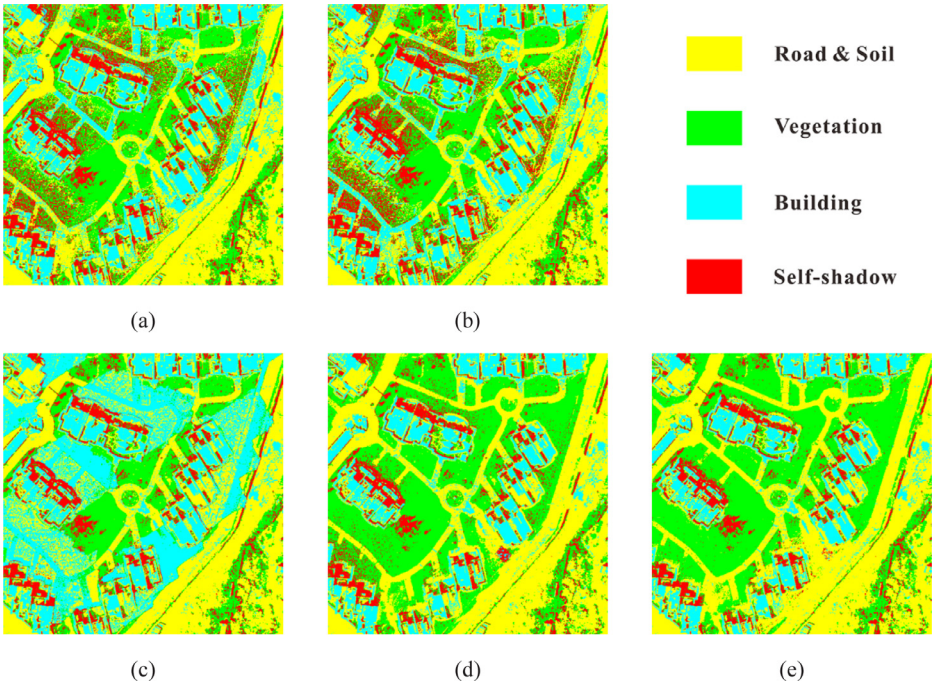

Fig. 11. Supervised classification of the shadow removal results in Fig. 5. (a) Result of the LCC method. (b) Result of the HMC method. (c) Result of the SMIT method. (d) Result of the SANL method. (e) Result of the proposed method. (For interpretation of the references to color in this figure, the reader is referred to the web version of this article.)

Table 2
Classification accuracy evaluation for selected samples from the shadow regions.

Method	Class	PA (%)	UA (%)	OA (%)	KC
LCC	Road and soil	47.32	65.07	65.13	0.5248
	Vegetation	61.09	97.69		
HMC	Road and soil	44.58	52.99	59.04	0.4507
	Vegetation	49.07	97.62		
SMIT	Road and soil	11.36	15.76	31.91	0.1044
	Vegetation	9.07	55.82		
SANL	Road and soil	96.47	**92.37**	94.16	0.9139
	Vegetation	95.10	98.24		
Proposed	Road and soil	**97.67**	92.15	**96.29**	**0.9448**
	Vegetation	**99.16**	**98.30**		

results in Fig. 11. The classification accuracies for the three images are listed in Table 2. Fig. 11 contains five land-cover types, i.e., road and soil (in yellow), vegetation (in green), building (in cyan), and self-shadow (in red). In Fig. 11(a) and (b), we can see that most of the land cover in the shadow regions has been correctly classified, but part of the road in the shadow regions is misclassified as building, and some scattered shadow regions exist in the results of the LCC method and HMC method. In Fig. 11(c), some road and vegetation regions in the shadow regions are misclassified as building because of the mismatching correction in the result of the SMIT method. In Fig. 11(d), the SANL method obtains a good classification result, but some small shadow pieces still exist. In Fig. 11(e), the land-cover types in the shadow regions are well classified into the correct categories, i.e., the vegetation and the road in the shadow regions have been properly identified, without obvious scattered shadow regions. Although some self-shadow regions still exist in the result of the proposed method, we mainly focus on cast shadow removal in this paper.

Classification accuracy evaluation was undertaken in selected samples by visual inspection, where all five methods used the same verification samples. From Table 2, in the results of the LCC, HMC, and SMIT methods, although the UA values of vegetation for the LCC and HMC methods are 97.69% and 97.62%, respectively, the PA and OA values are less than 66%, and the KC is less than 0.53, while in the results of SANL and the proposed method, the values of these three accuracy indices are all above 90%, and the KC is between 0.91 and 0.95. Compared to the SANL method, it is clear that the proposed method can achieve higher values in all the indices, except for the UA of road and soil, where there is a minor difference of 0.22%. From the above quantitative analysis, the proposed method obtains the best shadow removal result.

The classification accuracy evaluation for the selected samples from the three shadow images is shown in Table 3. The OA and KC are adopted as the evaluation indices. The accuracy of the pro-

Table 3
Classification accuracy evaluation for selected samples from the three shadow images.

Image	Index	LCC	HMC	SMIT	SANL	Proposed
#1	OA (%)	65.13	59.04	31.91	94.16	**96.29**
	KC	0.5248	0.4507	0.1044	0.9139	**0.9448**
#2	OA (%)	81.10	58.92	66.20	91.21	**94.27**
	KC	0.7063	0.4031	0.4305	0.8576	**0.9068**
#3	OA (%)	80.36	72.37	50.52	80.58	**97.75**
	KC	0.7332	0.6257	0.2592	0.7342	**0.9678**

Table 4
Computation time comparisons for shadow removal (in seconds) with three different shadow images.

Image size	LCC	HMC	SMIT	SNAL	Proposed
#1: 594 × 594	0.995	1.293	153.152	163.722	138.307
#2: 503 × 503	0.882	0.962	107.206	114.175	79.266
#3: 584 × 584	0.962	1.102	157.342	156.253	105.710

posed method is higher than that of the other four methods. The OA of the proposed method is between 94% and 97%, and the KC of the proposed method is between 0.90 and 0.97, which demonstrates its superiority.

Considering the efficiency of the different methods, the running time is also counted and listed in Table 4. Specifically, the SMIT method is realized with C++ programming language by the authors, while the other methods are all realized with Matlab. In general, C++ code shows superior performance better in time complexity than an equivalent Matlab implementation. As we can see, in most case, the computational time is proportional to the image size, except for image #3 with the SMIT method. It takes about 157.342 s longer than 153.152 s for image #1, because image #3 contains more complex land-cover types than image #1, and the subregion pairs matching spends more time. The LCC and HMC methods take about one second to remove the shadows for all these three images, significantly faster than the other three methods. These two methods are based on the simple statistical information without consideration of the different land-cover types in shadow regions and artifacts around the shadow boundaries in the shadow removal results. On the other hand, comparing with the SMIT and SNAL methods, the proposed method is the fastest for these three images. There is still a large space to accelerate the optimization and we will consider some speedup strategies, such as the multi-resolution scheme in the future [57].

4. Conclusion

In this paper, we have presented a novel shadow removal method based on separated illumination correction for urban aerial remote sensing images. The spatially adaptive weighted total variation (SAWTV) model is constructed to separate the structured illumination containing the shadow information and the shadow-free reflectance. The structured illumination is corrected by taking the land cover into consideration with object identification to preserve the clear edges of the land-cover types in the corrected shadow regions. As the structured illumination is piecewise smooth, the correction of the structured illumination can avoid the error caused by complex land cover more effectively, compared to undertaking correction on the observed image directly. From the visual comparison of the experimental results, the shadow regions corrected by the proposed method are more natural in visual appearance and are more consistent with their surroundings, compared to the results of the other four shadow removal methods. Two different quantitative assessment techniques also verified the superiority of the proposed method: the SSDI of the proposed method is distinctly lower than that of the other existing methods, and the classification OA and the KC of the proposed method are between 94% and 97% and 0.90 and 0.97, respectively, based on the SVM classification method.

Declaration of interests

The authors declare that they have no known competing financial interests or personal relationships that could have appeared to influence the work reported in this paper.

Acknowledgments

This work was supported by the National Natural Science Foundation of China (41401396 and 41871246) and the Key Program of the National Natural Science Foundation of China (41631180). The authors would like to thank the editors and the anonymous reviewers for their valuable suggestions.

References

[1] K.R.M. Adeline, M. Chen, X. Briottet, S.K. Pang, N. Paparoditis, Shadow detection in very high spatial resolution aerial images: a comparative study, ISPRS J. Photogramm. Remote Sens 80 (2013) 21–38.
[2] W. Zhou, G. Huang, A. Troy, M.L. Cadenasso, Object-based land cover classification of shaded areas in high spatial resolution imagery of urban areas: a comparison study, Remote Sens. Environ. 113 (8) (2009) 1769–1777.
[3] V. Arévalo, J. González, G. Ambrosio, Shadow detection in colour high-resolution satellite images, Int. J. Remote Sens. 29 (7) (2008) 1945–1963.
[4] D. Chai, S. Newsam, H.K. Zhang, Y. Qiu, J. Huang, Cloud and cloud shadow detection in landsat imagery based on deep convolutional neural networks, Remote Sens. Environ. 225 (2019) 307–316.
[5] Z. Li, H. Shen, H. Li, G. Xia, P. Gamba, L. Zhang, Multi-feature combined cloud and cloud shadow detection in GaoFen-1 wide field of view imagery, Remote Sens. Environ. 191 (2017) 342–358.
[6] S. Luo, H. Li, H. Shen, Shadow removal based on clustering correction of illumination field for urban aerial remote sensing images, in: Proceedings of the IEEE International Conference on Image Processing (ICIP), 2017, pp. 485–489.
[7] H. Zhang, K. Sun, W. Li, Object-oriented shadow detection and removal from urban high-resolution remote sensing images, IEEE Trans. Geosci. Remote Sens. 52 (11) (2014) 6972–6982.
[8] E. Maltezos, A. Doulamis, C. Ioannidis, Improving the visualisation of 3D textured models via shadow detection and removal, in: Proceedings of the 9th International Conference on Virtual Worlds and Games for Serious Applications (VS-Games), 2017, pp. 161–164.
[9] S.H. Khan, M. Bennamoun, F. Sohel, R. Togneri, Automatic shadow detection and removal from a single image, IEEE Trans. Pattern Anal. Mach. Intell. 38 (3) (2016) 431–446.
[10] V. Nguyen, T.F.Y. Vicente, M. Zhao, M. Hoai, D. Samaras, Shadow detection with conditional generative adversarial networks, in: Proceedings of the IEEE International Conference on Computer Vision (ICCV), 2017, pp. 4520–4528.
[11] P.M. Dare, Shadow analysis in high-resolution satellite imagery of urban areas, Photogramm. Eng. Remote Sens. 71 (2) (2005) 169–177.
[12] X. Kang, Y. Huang, S. Li, H. Lin, J.A. Benediktsson, Extended random walker for shadow detection in very high resolution remote sensing images, IEEE Trans. Geosci. Remote Sens. 56 (2) (2018) 867–876.
[13] N. Mo, R. Zhu, L. Yan, Z. Zhao, Deshadowing of urban airborne imagery based on object-oriented automatic shadow detection and regional matching compensation, IEEE J. Sel. Top. Appl. Earth Obs. Remote Sens. 11 (2) (2018) 585–605.
[14] N. Su, Y. Zhang, S. Tian, Y. Yan, X. Miao, Shadow detection and removal for occluded object information recovery in urban high-resolution panchromatic satellite images, IEEE J. Sel. Top. Appl. Earth Obs. Remote Sens. 9 (6) (2016) 2568–2582.
[15] P. Sarabandi, F. Yamazaki, M. Matsuoka, A. Kiremidjian, Shadow detection and radiometric restoration in satellite high resolution images, in: Proceedings of the IEEE International Geoscience and Remote Sensing Symposium (IGARSS), 2004, pp. 3744–3747.
[16] W. Liu, F. Yamazaki, Object-based shadow extraction and correction of high-resolution optical satellite images, IEEE J. Sel. Top. Appl. Earth Obs. Remote Sens. 5 (4) (2012) 1296–1302.
[17] L. Lorenzi, F. Melgani, G. Mercier, A complete processing chain for shadow detection and reconstruction in VHR images, IEEE Trans. Geosci. Remote Sens. 50 (9) (2012) 3440–3452.
[18] C. Xiao, D. Xiao, L. Zhang, L. Chen, Efficient shadow removal using subregion matching illumination transfer, Comput. Graph. Forum 32 (7) (2013) 421–430.
[19] A. Movia, A. Beinat, F. Crosilla, Shadow detection and removal in RGB VHR images for land use unsupervised classification, ISPRS J. Photogramm. Remote Sens. 119 (2016) 485–495.
[20] R. Guo, Q. Dai, D. Hoiem, Paired regions for shadow detection and removal, IEEE Trans. Pattern Anal. Mach. Intell. 35 (12) (2013) 2956–2967.

[21] L. Zhang, Q. Zhang, C. Xiao, Shadow Remover: image shadow removal based on illumination recovering optimization, IEEE Trans. Image Process. 24 (11) (2015) 4623–4636.
[22] V.J.D. Tsai, A comparative study on shadow compensation of color aerial images in invariant color models, IEEE Trans. Geosci. Remote Sens. 44 (6) (2006) 1661–1671.
[23] T.F.Y. Vicente, M. Hoai, D. Samaras, Leave-one-out kernel optimization for shadow detection and removal, IEEE Trans. Pattern Anal. Mach. Intell. 40 (3) (2018) 682–695.
[24] A. Massalabi, H. Dong-Chen, G.B. Benie, E. Beaudry, Detecting information under and from shadow in panchromatic ikonos images of the city of sherbrooke, in: Proceedings of the IEEE International Geoscience and Remote Sensing Symposium (IGARSS), 2004, pp. 2000–2003.
[25] Q. Zhan, W. Shi, Y. Xiao, Quantitative analysis of shadow effects in high-resolution images of urban areas, in: Proceedings of the International Archives Photogrammetry, Remote Sensing and Spatial Information Sciences, 2005 8/W27.
[26] Y. Li, P. Gong, T. Sasagawa, Integrated shadow removal based on photogrammetry and image analysis, Int. J. Remote Sens. 26 (18) (2005) 3911–3929.
[27] H. Song, B. Huang, K. Zhang, Shadow detection and reconstruction in high-resolution satellite images via morphological filtering and example-based learning, IEEE Trans. Geosci. Remote Sens. 52 (5) (2014) 2545–2554.
[28] G.D. Finlayson, S.D. Hordley, L. Cheng, M.S. Drew, On the removal of shadows from images, IEEE Trans. Pattern Anal. Mach. Intell. 28 (1) (2006) 59–68.
[29] G.D. Finlayson, M.S. Drew, C. Lu, Entropy minimization for shadow removal, Int. J. Comput. Vision. 85 (1) (2009) 35–57.
[30] F. Liu, M. Gleicher, Texture-consistent shadow removal, in: Proceedings of the European Conference on Computer Vision (ECCV), 2008, pp. 437–450.
[31] Y.F. Su, H.H. Chen, A three-stage approach to shadow field estimation from partial boundary information, IEEE Trans. Image Process. 19 (10) (2010) 2749–2760.
[32] E. Arbel, H. Hel-Or, Shadow removal using intensity surfaces and texture anchor points, IEEE Trans. Pattern Anal. Mach. Intell. 33 (6) (2011) 1202–1216.
[33] H. Li, L. Zhang, H. Shen, An adaptive nonlocal regularized shadow removal method for aerial remote sensing images, IEEE Trans. Geosci. Remote Sens. 52 (1) (2014) 106–120.
[34] J. Wang, X. Li, J. Yang, Stacked conditional generative adversarial networks for jointly learning shadow detection and shadow removal, in: Proceedings of the IEEE Conference on Computer Vision and Pattern Recognition (CVPR), 2018, pp. 1788–1797.
[35] L. Qu, J. Tian, S. He, Y. Tang, R.W.H. Lau, DeshadowNet: a Multi-context embedding deep network for shadow removal, in: Proceedings of the IEEE Conference on Computer Vision and Pattern Recognition (CVPR), 2017, pp. 2308–2316.
[36] X. Hu, C.-W. Fu, L. Zhu, J. Qin, P.-A. Heng, Direction-aware spatial context features for shadow detection and removal, arXiv:1805.04635, 2018.
[37] A. Levin, D. Lischinski, Y. Weiss, A closed-form solution to natural image matting, IEEE Trans. Pattern Anal. Mach. Intell. 30 (2) (2008) 228–242.
[38] E.H. Land, J.J. McCann, Lightness and retinex theory, J. Opt. Soc. Am. 61 (1) (1971) 1–11.
[39] H. Shen, X. Li, Q. Cheng, C. Zeng, G. Yang, H. Li, L. Zhang, Missing information reconstruction of remote sensing data: a technical review, IEEE Geosci. Remote Sens. Mag. 3 (3) (2015) 61–85.
[40] C. Zeng, H. Shen, L. Zhang, Recovering missing pixels for landsat ETM+ SLC-off imagery using multi-temporal regression analysis and a regularization method, Remote Sens. Environ. 131 (2013) 182–194.
[41] L. Yue, H. Shen, J. Li, Q. Yuan, H. Zhang, L. Zhang, Image super-resolution: the techniques, applications, and future, Signal Process 128 (2016) 389–408.
[42] H. Li, L. Zhang, H. Shen, A perceptually inspired variational method for the uneven intensity correction of remote sensing images, IEEE Trans. Geosci. Remote Sens. 50 (8) (2012) 3053–3065.
[43] M.K. Ng, W. Wang, A total variation model for retinex, SIAM J. Imag. Sci. 4 (1) (2011) 345–365.
[44] Q. Yuan, L. Zhang, H. Shen, Hyperspectral image denoising employing a spectral–spatial adaptive total variation model, IEEE Trans. Geosci. Remote Sens. 50 (10) (2012) 3660–3677.
[45] X. Liu, H. Shen, Q. Yuan, X. Lu, C. Zhou, A universal destriping framework combining 1-D and 2-D variational optimization methods, IEEE Trans. Geosci. Remote Sens. 56 (2) (2018) 808–822.
[46] X. Lan, H. Shen, L. Zhang, Q. Yuan, A spatially adaptive retinex variational model for the uneven intensity correction of remote sensing images, Signal Process 101 (2014) 19–34.
[47] T. Goldstein, S. Osher, The split bregman method for L1-Regularized problems, SIAM J. Imag. Sci. 2 (2) (2009) 323–343.
[48] Y. Chen, D. Wen, L. Jing, P. Shi, Shadow information recovery in urban areas from very high resolution satellite imagery, Int. J. Remote Sens. 28 (15) (2007) 3249–3254.
[49] F.L. Gadallah, F. Csillag, E.J.M. Smith, Destriping multisensor imagery with moment matching, Int. J. Remote Sens. 21 (12) (2000) 2505–2511.
[50] R. Guo, Q. Dai, D. Hoiem, Single-image shadow detection and removal using paired regions, in: Proceedings of the IEEE Conference on Computer Vision and Pattern Recognition (CVPR), 2011, pp. 2033–2040.
[51] M. Gryka, M. Terry, G.J. Brostow, Learning to remove soft shadows, ACM Trans. Graph. 34 (5) (2015) 1–15.
[52] V. Vapnik, The Nature of Statistical Learning Theory, Springer, New York, 1995.
[53] M. Story, R.G. Congalton, Accuracy assessment: a user's perspective, Photogramm. Eng. Remote Sens. 52 (3) (1986) 397–399.
[54] G.M. Foody, Status of land cover classification accuracy assessment, Remote Sens. Environ. 80 (1) (2002) 185–201.
[55] E. Reinhard, M. Adhikhmin, B. Gooch, P. Shirley, Color transfer between images, IEEE Comput. Graphics Appl. 21 (5) (2001) 34–41.
[56] H. Shen, L. Zhang, A MAP-Based algorithm for destriping and inpainting of remotely sensed images, IEEE Trans. Geosci. Remote Sens. 47 (5) (2009) 1492–1502.
[57] H. Li, X. Wang, H. Shen, Q. Yuan, L. Zhang, An efficient multi-resolution variational retinex scheme for the radiometric correction of airborne remote sensing images, Int. J. Remote Sens. 37 (5) (2016) 1154–1172.